Ferroelectric Control of Spin Polarization

V. Garcia, *et al.*

Science **327**, 1106 (2010);
DOI: 10.1126/science.1184028

Most plausible is that π^0 decays are responsible for the gamma-ray emission, although the bremsstrahlung scenario cannot be ruled out completely. In order to fit the Fermi LAT spectrum with π^0-decay emission, a spectral break in the proton spectrum is needed at fairly low energy, around 10 GeV/c. One possible mechanism to explain the spectral break is that particles escape from their acceleration sites, that is, the SNR shells. Theories predict that very high energy particles above ~TeV can be confined only during the early stage of SNR evolution (*11*, *12*). Because W44 is a middle-aged SNR with estimated age of $\sim 2.0 \times 10^4$ years, most particles accelerated up to higher energies in the past could have escaped from its shell and cannot contribute to the gamma-ray emission we are observing now.

In the case of W44, the effect of particle escape can be enhanced because of the interaction between the shell and the dense, largely neutral molecular gas. Magnetic turbulence, which is required to confine and efficiently accelerate particles, is considered to be substantially damped. Thus, particles can easily escape from the shell at an earlier stage of SNR evolution (*30*) compared with the case where an SNR is expanding in a more rarefied medium. For W44, parts of the shock are expanding into clumps and interclump gas with densities of ~10 to ~100 cm^{-3} (*15*). The Fermi LAT spectrum indicates that the slow shock velocity (<500 km s^{-1}) and efficient damping can limit the maximum particle energy to a few GeV. Our results for W44 demonstrate the capability of the Fermi LAT for morphological and spectral studies of GeV emission from Galactic SNRs, which allow us to study the escape of energetic particles from SNR shells into interstellar space, the evolution of SNR shocks during the age of the SNR, and the impact of a dense environment.

References and Notes

1. R. Blandford, D. Eichler, *Phys. Rep.* **154**, 1 (1987).
2. M. A. Malkov, L. O'C. Drury, *Rep. Prog. Phys.* **64**, 429 (2001).
3. S. P. Reynolds, *Annu. Rev. Astron. Astrophys.* **46**, 89 (2008).
4. F. A. Aharonian *et al.*, *Nature* **432**, 75 (2004).
5. F. A. Aharonian *et al.*, *Astron. Astrophys.* **464**, 235 (2007).
6. F. A. Aharonian *et al.*, *Astrophys. J.* **661**, 236 (2007).
7. A. R. Bell, S. G. Lucek, *Mon. Not. R. Astron. Soc.* **321**, 433 (2001).
8. E. G. Berezhko, H. J. Völk, *Astron. Astrophys.* **492**, 695 (2008).
9. F. A. Aharonian, L. O'C. Drury, H. J. Völk, *Astron. Astrophys.* **285**, 645 (1994).
10. L. O'C. Drury, F. A. Aharonian, H. J. Völk, *Astron. Astrophys.* **287**, 959 (1994).
11. V. S. Ptuskin, V. N. Zirakashvili, *Astron. Astrophys.* **429**, 755 (2005).
12. S. Gabici, F. A. Aharonian, *Astrophys. J.* **665**, L131 (2007).
13. M. Seta *et al.*, *Astron. J.* **127**, 1098 (2004).
14. I. M. Hoffman, W. M. Goss, C. L. Brogan, M. J. Claussen, *Astrophys. J.* **627**, 803 (2005).
15. W. T. Reach, J. Rho, T. H. Jarrett, *Astrophys. J.* **618**, 297 (2005).
16. W. T. Reach *et al.*, *Astron. J.* **131**, 1479 (2006).
17. J. A. Esposito, S. D. Hunter, G. Kanbach, P. Sreekumar, *Astrophys. J.* **461**, 820 (1996).
18. W. B. Atwood *et al.*, *Astrophys. J.* **697**, 1071 (2009).
19. A. A. Abdo *et al.*, *Astrophys. J.* **183** (suppl.), 46 (2009).
20. A. Wolszczan, J. M. Cordes, R. J. Dewey, *Astrophys. J.* **372**, L99 (1991).
21. R. Petre, K. D. Kuntz, R. L. Shelton, *Astrophys. J.* **579**, 404 (2002).
22. D. A. Frail, E. B. Giacani, W. M. Goss, G. Dubner, *Astrophys. J.* **464**, L165 (1996).
23. Fermi Science Support Center, http://fermi.gsfc.nasa.gov/ssc/.
24. A. A. Abdo *et al.*, The first Fermi Large Area Telescope catalog of gamma-ray pulsars, http://arxiv.org/abs/0910.1608.
25. Although the analysis was performed by using events above 200 MeV, the quoted flux was obtained by extrapolating the best-fit function down to 100 MeV to make it easier to compare the value with past publications on GeV gamma-ray observations.
26. G. Castelletti, G. Dubner, C. Brogan, N. E. Kassim, *Astron. Astrophys.* **471**, 537 (2007).
27. A. M. Bykov, R. A. Chevalier, D. C. Ellison, Y. A. Uvarov, *Astrophys. J.* **538**, 203 (2000).
28. T. A. Porter, I. V. Moskalenko, A. W. Strong, *Astrophys. J.* **648**, L29 (2006).
29. O. C. de Jager, A. Mastichiadis, *Astrophys. J.* **482**, 874 (1997).
30. V. S. Ptuskin, V. N. Zirakashvili, *Astron. Astrophys.* **403**, 1 (2003).
31. D. J. Helfand, R. H. Becker, R. L. White, A. Fallon, S. Tuttle, *Astron. J.* **131**, 2525 (2006).
32. J. H. Buckley *et al.*, *Astron. Astrophys.* **329**, 639 (1998).
33. F. A. Aharonian *et al.*, *Astron. Astrophys.* **395**, 803 (2002).
34. A. A. Abdo *et al.*, *Astrophys. J.* **700**, L127 (2009).

35. The Fermi LAT Collaboration acknowledges support from a number of agencies and institutes for both development and the operation of the LAT as well as scientific data analysis. These include NASA and Department of Energy in the United States; CEA/Irfu, IN2P3/CNRS, and Centre National d'Études Spatiales in France; ASI, INFN, and INAF in Italy; Ministry of Education, Culture, Sports, Science, and Technology, High Energy Accelerator Research Organization (KEK) and JAXA in Japan; and the K. A. Wallenberg Foundation, the Swedish Research Council, and the National Space Board in Sweden.

Supporting Online Material

www.sciencemag.org/cgi/content/full/science.1182787/DC1
Materials and Methods
SOM Text
Figs. S1 and S2
References and Notes

2 October 2009; accepted 29 December 2009
Published online 7 January 2010;
10.1126/science.1182787
Include this information when citing this paper.

Ferroelectric Control of Spin Polarization

V. Garcia,[1] M. Bibes,[1]* L. Bocher,[2] S. Valencia,[3] F. Kronast,[3] A. Crassous,[1] X. Moya,[4] S. Enouz-Vedrenne,[5] A. Gloter,[2] D. Imhoff,[2] C. Deranlot,[1] N. D. Mathur,[4] S. Fusil,[1,6] K. Bouzehouane,[1] A. Barthélémy[1]

A current drawback of spintronics is the large power that is usually required for magnetic writing, in contrast with nanoelectronics, which relies on "zero-current," gate-controlled operations. Efforts have been made to control the spin-relaxation rate, the Curie temperature, or the magnetic anisotropy with a gate voltage, but these effects are usually small and volatile. We used ferroelectric tunnel junctions with ferromagnetic electrodes to demonstrate local, large, and nonvolatile control of carrier spin polarization by electrically switching ferroelectric polarization. Our results represent a giant type of interfacial magnetoelectric coupling and suggest a low-power approach for spin-based information control.

Controlling the spin degree of freedom by purely electrical means is currently an important challenge in spintronics (*1*, *2*). Approaches based on spin-transfer torque (*3*) have proven very successful in controlling the direction of magnetization in a ferromagnetic layer, but they require the injection of high current densities. An ideal solution would rely on the application of an electric field across an insulator, as in existing nanoelectronics. Early experiments have demonstrated the volatile modulation of spin-based properties with a gate voltage applied through a dielectric. Notable examples include the gate control of the spin-orbit interaction in III-V quantum wells (*4*), the Curie temperature T_C (*5*), or the magnetic anisotropy (*6*) in magnetic semiconductors with carrier-mediated exchange interactions; for example, (Ga,Mn)As or (In,Mn)As. Electric field–induced modifications of magnetic anisotropy at room temperature have also been reported recently in ultrathin Fe-based layers (*7*, *8*).

[1]Unité Mixte de Physique CNRS/Thales, 1 Avenue Augustin Fresnel, Campus de l'Ecole Polytechnique, 91767 Palaiseau, France, and Université Paris-Sud, 91405 Orsay, France. [2]Laboratoire de Physique des Solides, Université Paris-Sud, CNRS UMR-8502, 91405 Orsay, France. [3]Helmholtz-Zentrum-Berlin, Berliner Elektronen-Speicherring Gesellschaft für Synchrotronstrahlung (BESSY), Albert-Einstein-Strasse 15,12489 Berlin, Germany. [4]Department of Materials Science, University of Cambridge, Cambridge, CB2 3QZ, UK. [5]Thales Research and Technology, 1 Avenue Augustin Fresnel, Campus de l'Ecole Polytechnique, 91767 Palaiseau, France. [6]Université d'Evry-Val d'Essonne, Boulevard François Mitterrand, 91025 Evry cedex, France.

*To whom correspondence should be addressed. E-mail: manuel.bibes@thalesgroup.com

A nonvolatile extension of this approach involves replacing the gate dielectric by a ferroelectric and taking advantage of the hysteretic response of its order parameter (polarization) with an electric field. When combined with (Ga, Mn)As channels, for instance, a remanent control of T_C over a few kelvin was achieved through polarization-driven charge depletion/accumulation (*9*, *10*), and the magnetic anisotropy was modified by the coupling of piezoelectricity and magnetostriction (*11*, *12*). Indications of an electrical control of magnetization have also been provided in magnetoelectric heterostructures at room temperature (*13*–*17*).

Recently, several theoretical studies have predicted that large variations of magnetic properties may occur at interfaces between ferroelectrics and high-T_C ferromagnets such as Fe (*18*–*20*), Co_2MnSi (*21*), or Fe_3O_4 (*22*). Changing the direction of the ferroelectric polarization has been predicted to influence not only the interfacial anisotropy and magnetization, but also the spin polarization. Spin polarization [i.e., the normalized difference in the density of states (DOS) of majority and minority spin carriers at the Fermi level (E_F)] is typically the key parameter controlling the response of spintronics systems, epitomized by magnetic tunnel junctions in which the tunnel magnetoresistance (*TMR*) is related to the electrode spin polarization by the Jullière formula (*23*). These predictions suggest that the nonvolatile character of ferroelectrics at the heart of ferroelectric random access memory technology (*24*) may be exploited in spintronics devices such as magnetic random access memories or spin field-effect transistors (*2*). However, the nonvolatile electrical control of spin polarization has not yet been demonstrated.

We address this issue experimentally by probing the spin polarization of electrons tunneling from an Fe electrode through ultrathin ferroelectric $BaTiO_3$ (BTO) tunnel barriers (Fig. 1A). The BTO polarization can be electrically switched to point toward or away from the Fe electrode. We used a half-metallic $La_{0.67}Sr_{0.33}MnO_3$ (LSMO) (*25*) bottom electrode as a spin detector in these artificial multiferroic tunnel junctions (*26*, *27*). Magnetotransport experiments provide evidence for a large and reversible dependence of the *TMR* on ferroelectric polarization direction.

The tunnel junctions that we used in this study are based on BTO(1 nm)/LSMO(30 nm) bilayers grown epitaxially onto (001)-oriented $NdGaO_3$ (NGO) single-crystal substrates (*28*). The large (~180°) and stable piezoresponse force microscopy (PFM) phase contrast (*28*) between negatively and positively poled areas (Fig. 1B, top) indicates that the ultrathin BTO films are ferroelectric at room temperature (*29*). The persistence of ferroelectricity for such ultrathin films of BTO arises from the large lattice mismatch with the NGO substrate (–3.2%), which is expected to dramatically enhance ferroelectric properties in this highly strained BTO (*30*). The local topographical and transport properties of the BTO(1 nm)/LSMO(30 nm) bilayers were characterized by conductive-tip atomic force microscopy (CTAFM) (*28*). The surface is very smooth with terraces separated by one-unit-cell–high steps, visible in both the topography (*29*) and resistance mappings (Fig. 1B, bottom). No anomalies in the CTAFM data were observed over lateral distances on the micrometer scale.

We defined tunnel junctions from these bilayers by a lithographic technique based on CTAFM (*28*, *31*). Top electrical contacts of diameter ~10 to 30 nm can be patterned by this nanofabrication process. The subsequent sputter deposition of a 5-nm-thick Fe layer, capped by a

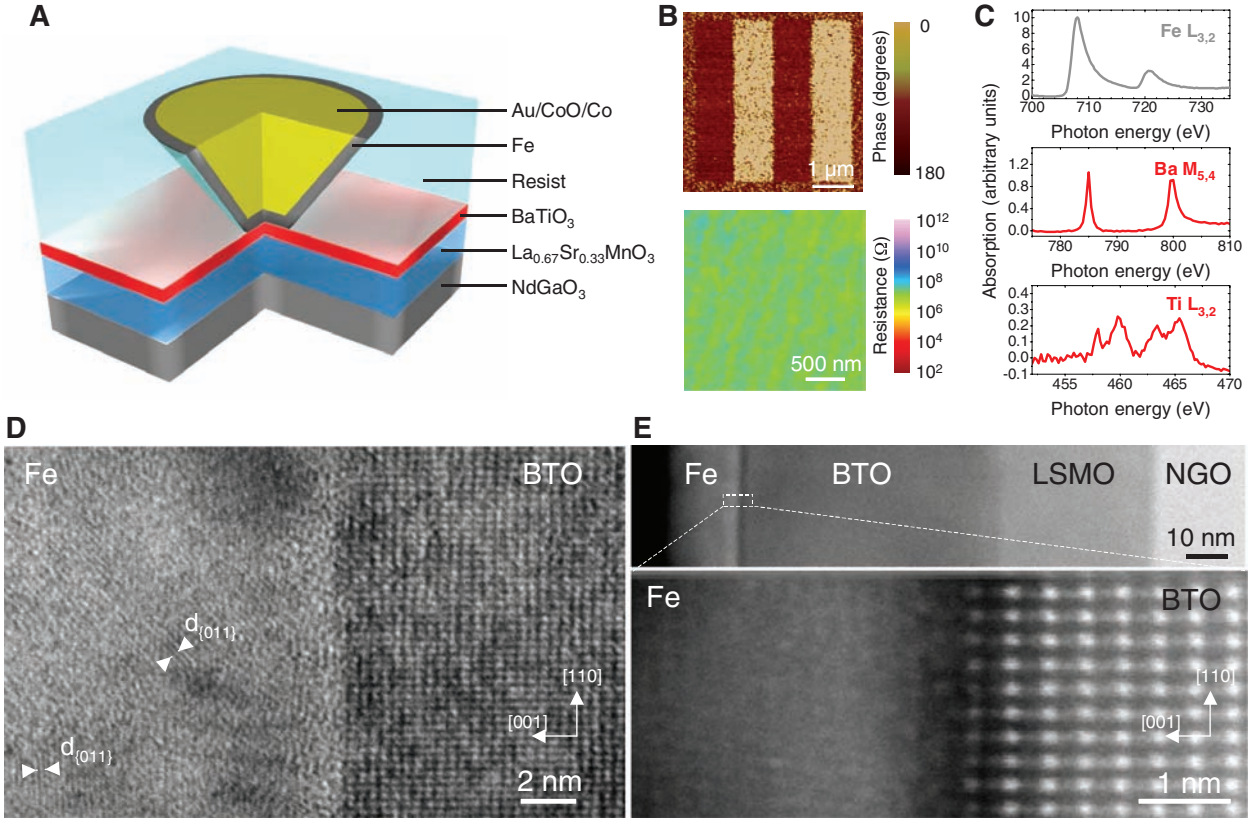

Fig. 1. (**A**) Sketch of the nanojunction defined by electrically controlled nanoindentation. A thin resist is spin-coated on the BTO(1 nm)/LSMO(30 nm) bilayer. The nanoindentation is performed with a conductive-tip atomic force microscope, and the resulting nano-hole is filled by sputter-depositing Au/CoO/Co/Fe. (**B**) (Top) PFM phase image of a BTO(1 nm)/LSMO(30 nm) bilayer after poling the BTO along 1-by-4–μm stripes with either a negative or positive (tip-LSMO) voltage. (Bottom) CTAFM image of an unpoled area of a BTO(1 nm)/LSMO(30 nm) bilayer. Ω, ohms. (**C**) X-ray absorption spectra collected at room temperature close to the Fe $L_{3,2}$ (top), Ba $M_{5,4}$ (middle), and Ti $L_{3,2}$ (bottom) edges on an AlO_x(1.5 nm)/Al(1.5 nm)/Fe(2 nm)/BTO(1 nm)/LSMO(30 nm)//NGO(001) heterostructure. (**D**) HRTEM and (**E**) HAADF images of the Fe/BTO interface in a Ta(5 nm)/Fe(18 nm)/BTO(50 nm)/LSMO(30 nm)//NGO(001) heterostructure. The white arrowheads in (D) indicate the lattice fringes of {011} planes in the iron layer. [110] and [001] indicate pseudotetragonal crystallographic axes of the BTO perovskite.

Au(100 nm)/CoO(3.5 nm)/Co(11.5 nm) stack to increase coercivity, defined a set of nanojunctions (Fig. 1A). The same Au/CoO/Co/Fe stack was deposited on another BTO(1 nm)/LSMO(30 nm) sample for magnetic measurements. Additionally, a Ta(5 nm)/Fe(18 nm)/BTO(50 nm)/LSMO(30 nm) sample and a AlO_x(1.5 nm)/Al(1.5 nm)/Fe(2 nm)/BTO(1 nm)/LSMO(30 nm) sample were realized for structural and spectroscopic characterizations.

We used both a conventional high-resolution transmission electron microscope (HRTEM) and the NION UltraSTEM 100 scanning transmission electron microscope (STEM) to investigate the Fe/BTO interface properties of the Ta/Fe/BTO/LSMO sample. The epitaxial growth of the BTO/LSMO bilayer on the NGO substrate was confirmed by HRTEM and high-resolution STEM images. The low-resolution, high-angle annular dark field (HAADF) image of the entire heterostructure shows the sharpness of the LSMO/BTO interface over the studied area (Fig. 1E, top). Figure 1D reveals a smooth interface between the BTO and the Fe layers. Whereas the BTO film is epitaxially grown on top of LSMO, the Fe layer consists of textured nanocrystallites. From the in-plane (a) and out-of-plane (c) lattice parameters in the tetragonal BTO layer, we infer that $c/a = 1.016 \pm 0.008$, in good agreement with the value of 1.013 found with the use of x-ray diffraction (*29*). The interplanar distances for selected crystallites in the Fe layer [i.e., ~2.03 Å (Fig. 1D, white arrowheads)] are consistent with the {011} planes of body-centered cubic (bcc) Fe.

We investigated the BTO/Fe interface region more closely in the HAADF mode of the STEM (Fig. 1E, bottom). On the BTO side, the atomically resolved HAADF image allows the distinction of atomic columns where the perovskite A-site atoms (Ba) appear as brighter spots. Lattice fringes with the characteristic {100} interplanar distances of bcc Fe (~2.86 Å) can be distinguished on the opposite side. Subtle structural, chemical, and/or electronic modifications may be expected to occur at the interfacial boundary between the BTO perovskite-type structure and the Fe layer. These effects may lead to interdiffusion of Fe, Ba, and O atoms over less than 1 nm, or the local modification of the Fe DOS close to E_F, consistent with ab initio calculations of the BTO/Fe interface (*18*–*20*).

To characterize the oxidation state of Fe, we performed x-ray absorption spectroscopy (XAS) measurements on a AlO_x(1.5 nm)/Al(1.5 nm)/Fe(2 nm)/BTO(1 nm)/LSMO(30 nm) sample (*28*). The probe depth was at least 7 nm, as indicated by the finite XAS intensity at the La $M_{4,5}$ edge (*28*), so that the entire Fe thickness contributed substantially to the signal. As shown in Fig. 1C (top), the spectrum at the Fe $L_{2,3}$ edge corresponds to that of metallic Fe (*32*). The XAS spectrum obtained at the Ba $M_{4,5}$ edge (Fig. 1C, middle) is similar to that reported for Ba^{2+} in (*33*). Despite the poor signal-to-noise ratio, the Ti $L_{2,3}$ edge spectrum (Fig. C, bottom) shows the typical signature expected for a valence close to 4+ (*34*). From the XAS, HRTEM, and STEM analyses, we conclude that the Fe/BTO interface is smooth with no detectable oxidation of the Fe layer within a limit of less than 1 nm.

After cooling in a magnetic field of 5 kOe aligned along the [110] easy axis of pseudocubic LSMO (which is parallel to the orthorhombic [100] axis of NGO), we characterized the transport properties of the junctions at low temperature (4.2 K). Figure 2A (middle) shows a typical resistance–versus–magnetic field $R(H)$ cycle recorded at a bias voltage of –2 mV (positive bias corresponds to electrons tunneling from Fe to LSMO). The bottom panel of Fig. 2A shows the magnetic hysteresis loop $m(H)$ of a similar unpatterned sample measured with superconducting quantum interference device (SQUID) magnetometry. When we decreased the magnetic field from a large positive value, the resistance dropped in the –50 to –250 Oe range and then followed a plateau down to –800 Oe, after which it sharply returned to the high-resistance state. We observed a similar response when cycling the field back to large positive values. A comparison with the $m(H)$ loop indicates that the switching fields in $R(H)$ correspond to changes in the relative magnetic configuration of the LSMO and Fe electrodes from parallel (at high field) to antiparallel (at low field). The magnetically softer LSMO layer switched at lower fields (50 to 250 Oe) compared with the Fe layer, for which coupling to the exchange-biased Co/CoO induces larger and asymmetric coercive fields (–800 Oe, 300 Oe). The observed $R(H)$ corresponds to a negative $TMR = (R_{ap} - R_p)/R_{ap}$ of –17% [R_p and R_{ap} are the resistance in the parallel (p) and antiparallel (ap) magnetic configurations, respectively; see the sketches in Fig. 2A]. Within the simple Jullière model of TMR (*23*) and considering the large positive spin polarization of half-metallic LSMO (*25*), this negative TMR corresponds to a negative spin polarization for bcc Fe at the interface with BTO, in agreement with ab initio calculations (*18*–*20*).

As predicted (*35*–*38*) and demonstrated (*29*) previously, the tunnel current across a ferroelectric barrier depends on the direction of the ferroelectric polarization. We also observed this effect in our Fe/BTO/LSMO junctions. As can be seen in Fig. 2B, after poling the BTO at 4.2 K to orient its polarization toward LSMO or Fe (with a poling voltage of $VP- \approx -1$ V or $VP+ \approx 1$ V, respectively; see Fig. 2B sketches), current-versus-voltage $I(V_{DC})$ curves collected at low bias voltages showed a finite difference corresponding to a tunnel electroresistance as large as $TER = (I_{VP+} - I_{VP-})/I_{VP-} \approx 37\%$ (Fig. 2B, inset). This TER can be interpreted within an electrostatic model (*36*–*39*), taking into account the asymmetric deformation

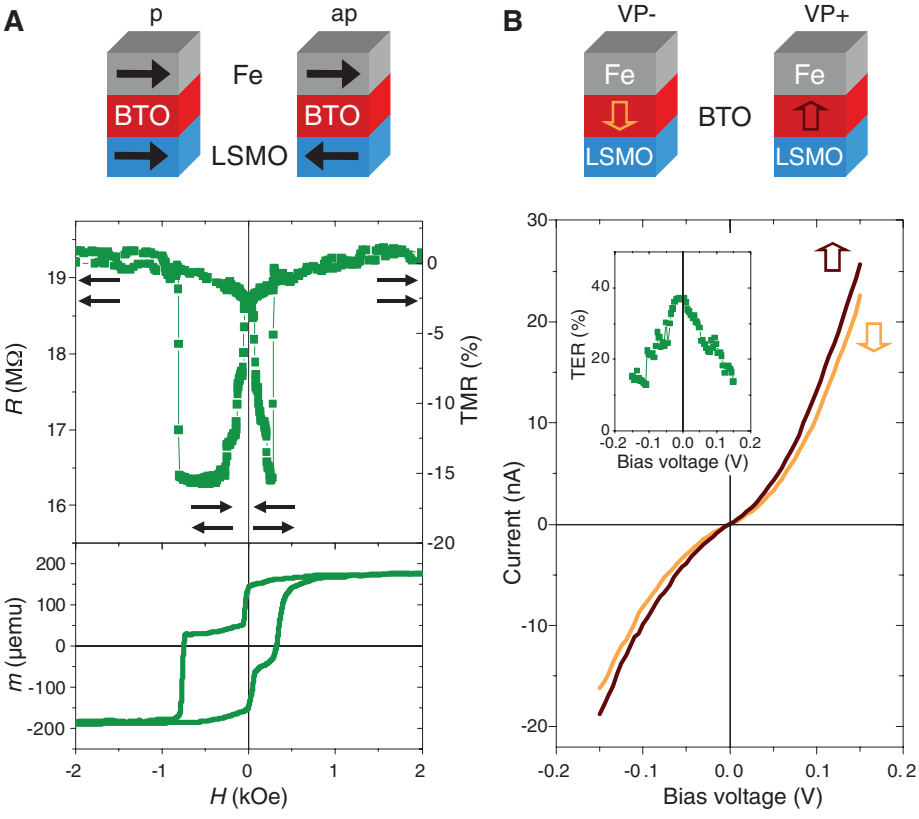

Fig. 2. (**A**) (Top) Device schematic with black arrows to indicate magnetizations. p, parallel; ap, antiparallel. (Middle) $R(H)$ recorded at –2 mV and 4.2 K showing negative TMR. (Bottom) $m(H)$ recorded at 30 K with a SQUID magnetometer. emu, electromagnetic units. (**B**) (Top) Device schematic with arrows to indicate ferroelectric polarization. (Bottom) $I(V_{DC})$ curves recorded at 4.2 K after poling the ferroelectric down (orange curve) or up (brown curve). The bias dependence of the TER is shown in the inset.

of the barrier potential profile that is created by the incomplete screening of polarization charges by different Thomas-Fermi screening lengths at Fe/BTO and LSMO/BTO interfaces. Piezoelectric-related *TER* effects (*35*, *38*) can be neglected as the piezoelectric coefficient estimated from PFM experiments is too small in our clamped films (*29*). *TER* measurements performed on a BTO(1 nm)/LSMO(30 nm) bilayer with the use of a CTAFM boron-doped diamond tip as the top electrode showed values of ~200% (*29*). Given the strong sensitivity of the *TER* on barrier parameters and barrier-electrode interfaces, these two values are not expected to match precisely. We anticipate that the *TER* variation between Fe/BTO/LSMO junctions and CTAFM-based measurements is primarily the result of different electrostatic boundary conditions.

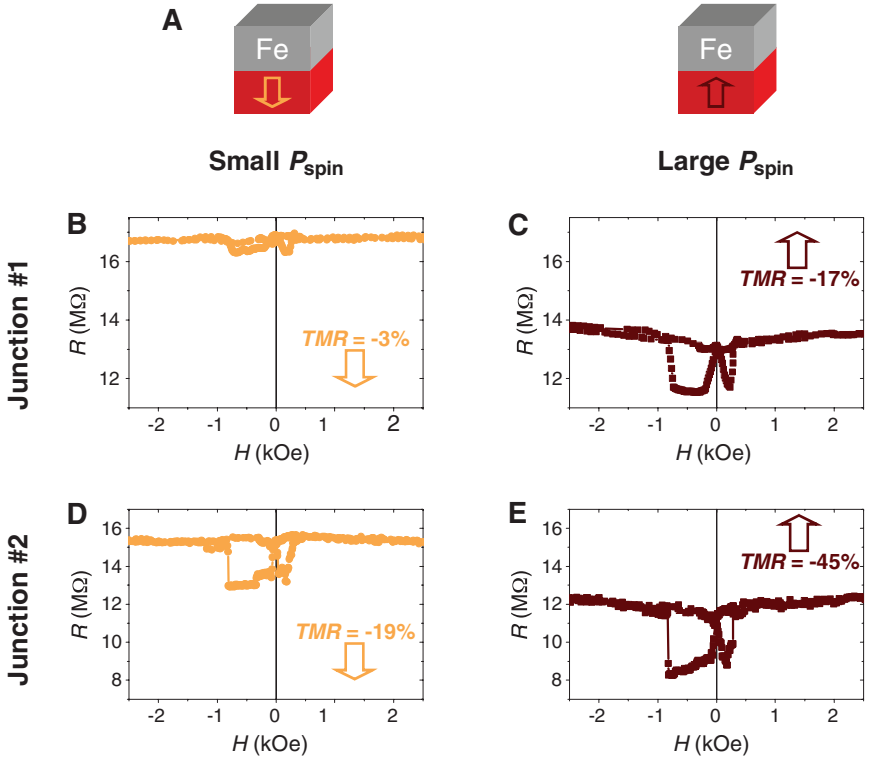

Fig. 3. (**A**) Sketch of the electrical control of spin polarization at the Fe/BTO interface. (**B** and **C**) *R*(*H*) curves for junction #1 (V_{DC} = –50 mV, *T* = 4.2 K) after poling the ferroelectric barrier down or up, respectively. (**D** and **E**) *R*(*H*) curves for junction #2 (V_{DC} = –50 mV, *T* = 4.2 K) after poling the ferroelectric barrier down or up, respectively.

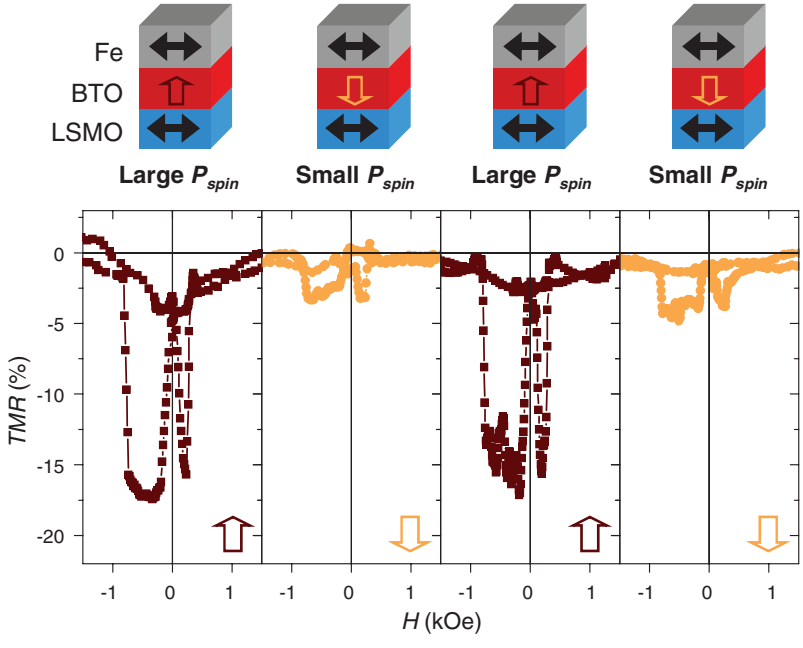

Fig. 4. *TMR*(*H*) curves recorded for junction #1 (V_{DC} = –50 mV, *T* = 4.2 K) after poling the ferroelectric up (*VP*+), down (*VP*–), up (*VP*+), and down (*VP*–).

Switching the ferroelectric polarization of a tunnel barrier with voltage pulses is also expected to affect the spin-dependent DOS of electrodes at a ferromagnet/ferroelectric interface. Interfacial modifications of the spin-dependent DOS of the half-metallic LSMO by the ferroelectric BTO are not likely, as no states are present for the minority spins up to ~350 meV above E_F (*40*, *41*). For 3d ferromagnets such as Fe, large modifications of the spin-dependent DOS are expected, as charge transfer between spin-polarized empty and filled states is possible. For the Fe/BTO interface, large changes have been predicted through ab initio calculations of 3d electronic states of bcc Fe at the interface with BTO by several groups (*18*–*20*).

To experimentally probe possible changes in the spin polarization of the Fe/BTO interface, we measured *R*(*H*) at a fixed bias voltage of –50 mV after aligning the ferroelectric polarization of BTO toward Fe or LSMO. *R*(*H*) cycles were collected for each direction of the ferroelectric polarization for two typical tunnel junctions of the same sample (Fig. 3, B and C, for junction #1; Fig. 3, D and E, for junction #2). In both junctions at the saturating magnetic field, high- and low-resistance states are observed when the ferroelectric polarization points toward LSMO or Fe, respectively, with a variation of ~ 25%. This result confirms the *TER* observations in Fig. 2B.

More interestingly, here, the *TMR* is dramatically modified by the reversal of BTO polarization. For junction #1, the *TMR* amplitude changes from –17 to –3% when the ferroelectric polarization is aligned toward Fe or LSMO, respectively (Fig. 3, B and C). Similarly for junction #2, the *TMR* changes from –45 to –19%. Similar results were obtained on Fe/BTO (1.2 nm)/LSMO junctions (*28*). Within the Jullière model (*23*), these changes in *TMR* correspond to a large (or small) spin polarization at the Fe/BTO interface when the ferroelectric polarization of BTO points toward (or away from) the Fe electrode. These experimental data support our interpretation regarding the electrical manipulation of the spin polarization of the Fe/BTO interface by switching the ferroelectric polarization of the tunnel barrier.

To quantify the sensitivity of the *TMR* with the ferroelectric polarization, we define a term, the tunnel electromagnetoresistance, as $TEMR = (TMR_{VP+} - TMR_{VP-})/TMR_{VP-}$. Large values for the *TEMR* are found for junctions #1 (450%) and #2 (140%), respectively. This electrical

control of the *TMR* with the ferroelectric polarization is repeatable, as shown in Fig. 4 for junction #1 where *TMR* curves are recorded after poling the ferroelectric up, down, up, and down, sequentially (*28*).

For tunnel junctions with a ferroelectric barrier and dissimilar ferromagnetic electrodes, we have reported the influence of the electrically controlled ferroelectric barrier polarization on the tunnel-current spin polarization. This electrical influence over magnetic degrees of freedom represents a new and interfacial magnetoelectric effect that is large because spin-dependent tunneling is very sensitive to interfacial details. Ferroelectrics can provide a local, reversible, nonvolatile, and potentially low-power means of electrically addressing spintronics devices.

References and Notes

1. C. Chappert, A. Fert, F. N. Van Dau, *Nat. Mater.* **6**, 813 (2007).
2. I. Žutić, J. Fabian, S. Das Sarma, *Rev. Mod. Phys.* **76**, 323 (2004).
3. J. C. Slonczewski, *J. Magn. Magn. Mater.* **159**, L1 (1996).
4. J. Nitta, T. Akazaki, H. Takayanagi, T. Enoki, *Phys. Rev. Lett.* **78**, 1335 (1997).
5. H. Ohno *et al.*, *Nature* **408**, 944 (2000).
6. D. Chiba *et al.*, *Nature* **455**, 515 (2008).
7. M. Weisheit *et al.*, *Science* **315**, 349 (2007).
8. T. Maruyama *et al.*, *Nat. Nanotechnol.* **4**, 158 (2008).
9. S. W. E. Riester *et al.*, *Appl. Phys. Lett.* **94**, 063504 (2009).
10. I. Stolichnov *et al.*, *Nat. Mater.* **7**, 464 (2008).
11. C. Bihler *et al.*, *Phys. Rev. B* **78**, 045203 (2008).
12. M. Overby, A. Chernyshov, L. P. Rokhinson, X. Liu, J. K. Furdyna, *Appl. Phys. Lett.* **92**, 192501 (2008).
13. C. Thiele, K. Dörr, O. Bilani, J. Rödel, L. Schultz, *Phys. Rev. B* **75**, 054408 (2007).
14. W. Eerenstein, M. Wiora, J. L. Prieto, J. F. Scott, N. D. Mathur, *Nat. Mater.* **6**, 348 (2007).
15. T. Kanki, H. Tanaka, T. Kawai, *Appl. Phys. Lett.* **89**, 242506 (2006).
16. Y.-H. Chu *et al.*, *Nat. Mater.* **7**, 478 (2008).
17. S. Sahoo *et al.*, *Phys. Rev. B* **76**, 092108 (2007).
18. C.-G. Duan, S. S. Jaswal, E. Y. Tsymbal, *Phys. Rev. Lett.* **97**, 047201 (2006).
19. M. Fechner *et al.*, *Phys. Rev. B* **78**, 212406 (2008).
20. J. Lee, N. Sai, T. Cai, Q. Niu, A. A. Demkov, preprint available at http://arxiv.org/abs/0912.3492v1.
21. K. Yamauchi, B. Sanyal, S. Picozzi, *Appl. Phys. Lett.* **91**, 062506 (2007).
22. M. K. Niranjan, J. P. Velev, C.-G. Duan, S. S. Jaswal, E. Y. Tsymbal, *Phys. Rev. B* **78**, 104405 (2008).
23. M. Jullière, *Phys. Lett. A* **54**, 225 (1975).
24. J. F. Scott, *Science* **315**, 954 (2007).
25. M. Bowen *et al.*, *Appl. Phys. Lett.* **82**, 233 (2003).
26. J. P. Velev *et al.*, *Nano Lett.* **9**, 427 (2009).
27. F. Yang *et al.*, *J. Appl. Phys.* **102**, 044504 (2007).
28. Materials and methods are available as supporting material on *Science* Online.
29. V. Garcia *et al.*, *Nature* **460**, 81 (2009).
30. K. J. Choi *et al.*, *Science* **306**, 1005 (2004).
31. K. Bouzehouane *et al.*, *Nano Lett.* **3**, 1599 (2003).
32. T. J. Regan *et al.*, *Phys. Rev. B* **64**, 214422 (2001).
33. N. Hollmann *et al.*, *Phys. Rev. B* **80**, 085111 (2009).
34. M. Abbate *et al.*, *Phys. Rev. B* **44**, 5419 (1991).
35. E. Y. Tsymbal, H. Kohlstedt, *Science* **313**, 181 (2006).
36. M. Ye. Zhuravlev, R. F. Sabirianov, S. S. Jaswal, E. Y. Tsymbal, *Phys. Rev. Lett.* **94**, 246802 (2005).
37. M. Ye. Zhuravlev, R. F. Sabirianov, S. S. Jaswal, E. Y. Tsymbal, *Phys. Rev. Lett.* **102**, 169901 (2009).
38. H. Kohlstedt, N. A. Pertsev, J. Rodriguez Contreras, R. Waser, *Phys. Rev. B* **72**, 125341 (2005).
39. M. Gajek *et al.*, *Nat. Mater.* **6**, 296 (2007).
40. M. Bowen *et al.*, *Phys. Rev. Lett.* **95**, 137203 (2005).
41. J. D. Burton, E. Y. Tsymbal, *Phys. Rev. B* **80**, 174406 (2009).

42. We thank R. Guillemet, C. Israel, M. E. Vickers, R. Mattana, J.-M. George, and P. Seneor for technical assistance, and C. Colliex for fruitful discussions on the microscopy measurements. This study was partially supported by the France-U.K. Partenariat Hubert Curien Alliance program, the French Réseau Thématique de Recherche Avancée Triangle de la Physique, the European Union (EU) Specific Targeted Research Project (STReP) Manipulating the Coupling in Multiferroic Films, EU STReP Controlling Mesoscopic Phase Separation, U.K. Engineering and Physical Sciences Research Council grant EP/E026206/I, French C-Nano Île de France, French Agence Nationale de la Recherche (ANR) Oxitronics, French ANR Alicante, the European Enabling Science and Technology through European Elelctron Microscopy program, and the French Microscopie Electronique et Sonde Atomique network. X.M. acknowledges support from Comissionat per a Universitats i Recerca (Generalitat de Catalunya).

Supporting Online Material

www.sciencemag.org/cgi/content/full/science.1184028/DC1
Materials and Methods
Figs. S1 to S5
References

30 October 2009; accepted 4 January 2010
Published online 14 January 2010;
10.1126/science.1184028
Include this information when citing this paper.

Integrated Catalytic Conversion of γ-Valerolactone to Liquid Alkenes for Transportation Fuels

Jesse Q. Bond, David Martin Alonso, Dong Wang, Ryan M. West, James A. Dumesic*

Efficient synthesis of renewable fuels remains a challenging and important line of research. We report a strategy by which aqueous solutions of γ-valerolactone (GVL), produced from biomass-derived carbohydrates, can be converted to liquid alkenes in the molecular weight range appropriate for transportation fuels by an integrated catalytic system that does not require an external source of hydrogen. The GVL feed undergoes decarboxylation at elevated pressures (e.g., 36 bar) over a silica/alumina catalyst to produce a gas stream composed of equimolar amounts of butene and carbon dioxide. This stream is fed directly to an oligomerization reactor containing an acid catalyst (e.g., H ZSM-5, Amberlyst-70), which couples butene monomers to form condensable alkenes with molecular weights that can be targeted for gasoline and/or jet fuel applications. The effluent gaseous stream of CO_2 at elevated pressure can potentially be captured and then treated or sequestered to mitigate greenhouse gas emissions from the process.

Diminishing fossil fuel resources and increasing amounts of CO_2 in the atmosphere require the development and implementation of strategies for the production of renewable transportation fuels (*1*–*4*). Although first-generation biofuels, such as corn ethanol and biodiesel, have the capacity to mitigate worldwide dependence on petroleum, new processes using lignocellulosic biomass must be developed to produce sustainable biofuels to meet worldwide demand (*5*). In this respect, γ-valerolactone (GVL) has been identified as a renewable platform molecule (*6*) with potential impact as a feedstock in the production of both energy (*6*, *7*) and fine chemicals (*8*). GVL is produced by hydrogenation of levulinic acid, which can be produced, potentially at low cost, from agricultural waste (*3*) by processes already demonstrated on a commercial scale (*9*). Recently, researchers have minimized the demand for an external source of hydrogen in this process by using the formic acid formed in equimolar amounts with levulinic acid through decomposition of cellulose (*7*) and C_6 sugars (*10*).

GVL retains 97% of the energy content of glucose and performs comparably to ethanol when used as a blending agent (10% v/v) in conventional gasoline (*6*). It has also been applied as a renewable cosolvent in splash blendable diesel fuel (*11*). GVL suffers, however, from several limitations for widespread use in the transportation sector, such as high water solubility, blending limits for use in conventional combustion engines, and lower energy density compared to petroleum-derived fuels. Although these limitations can be at least partially alleviated by reduction of GVL with an external source of hydrogen to produce methyltetrahydrofuran (*12*), which can be blended up to 70% in gasoline (*3*), the limitations would be completely eliminated by converting GVL to liquid alkenes (or alkanes) with molecular weights targeted for direct use as gasoline, jet, and/or diesel fuels.

Regarding the economic feasibility and environmental impact of biofuels, two commonly cited considerations are the demand for external hydrogen in producing a surrogate fuel and CO_2 emissions arising from its combustion (*13*). By processing GVL with a combined decarboxylation and oligomerization strategy, it is possible to

Department of Chemical and Biological Engineering, University of Wisconsin-Madison, Madison, WI 53706, USA.

*To whom correspondence should be addressed. E-mail: dumesic@engr.wisc.edu